ELSEVIER

Journal of Structural Geology 29 (2007) 1558–1570

JOURNAL OF STRUCTURAL GEOLOGY

www.elsevier.com/locate/jsg

Shape fabrics in populations of rigid objects in 2D: Estimating finite strain and vorticity

Kieran F. Mulchrone *

Department of Applied Mathematics, National University of Ireland, Cork, Ireland

Received 29 June 2006; received in revised form 6 June 2007; accepted 23 June 2007
Available online 18 July 2007

Abstract

Shape fabrics of elliptical objects in rocks are usually assumed to develop by passive behaviour of inclusions together with the surrounding material leading to shape-based strain analysis methods belonging to the R_f/ϕ family. By deriving the probability density function for populations of rigid ellipses deforming in a general 2D deformation, a method is developed which can be used to estimate both finite strain and the kinematic vorticity number. Statistical parameters are theoretically derived and their behaviours under various kinematic conditions are investigated. The maximum likelihood method from statistics is used to produce a numerical method for estimating deformation parameters from natural populations. A simulation study demonstrates that finite strain can be estimated well for both low and high applied finite strains, whereas the kinematic vorticity number is well estimated only in the case of high finite strains ($R_s > 40$), and that large sample numbers (≈ 1000) are required.

Keywords: Deformation; Shape fabric; Kinematic vorticity number; Rigid object; Probability distribution function

1. Introduction

Shape fabrics are a common feature of deformed rocks and are usually defined by elongate, approximately elliptical, clasts or porphyroblasts. The finite strain which leads to a shape fabric is usually estimated by applying the R_f/ϕ and related methods of strain analysis. A shared assumption of all these methods is that individual markers behaved passively during deformation. There are many instances where this is not the case and application of such methods can lead to erroneous results. Therefore the purpose of this paper is to develop a method which allows calculation of finite strain from a population of rigid objects. Additionally, as has been noted by previous workers (e.g. Masuda et al., 1995; Marques and Coelho, 2003), rigid object populations have the potential to allow for estimation of the flow type (i.e. kinematic vorticity number) that produced a particular distribution. Thus, the method developed in this paper may also be used to estimate the flow vorticity.

There has been considerable interest in the properties of populations rigid objects modified during deformation, most of which is underpinned by the landmark work of Jeffery (1922). Experimental work, both analogue and numerical, has served to advance our understanding of the behaviour of interacting populations of objects (see for example Ildefonse et al., 1992a,b; Arbaret et al., 1996; Jezek et al., 1996, 1999; Piazolo et al., 2002; Mulchrone et al., 2005). Fernandez et al. (1983, 1987) derived the theory of rigid object shape fabrics developed under 2D simple shear and observed the cyclical nature of such fabrics. Masuda et al. (1995) conducted an essentially numerical study whereby initially uniform distributions of rigid particles were deformed over a range of axial ratios and kinematic conditions. They found a gradual transition from symmetric to asymmetric distributions (when considered across all axial ratios) as the kinematics went from pure to simple shear, respectively. Recently, Marques and Coelho (2003) extended our understanding of the behaviour of rigid object populations by examining their behaviour under

* Tel.: +353 21 4903411.
E-mail address: k.mulchrone@ucc.ie

0191-8141/$ - see front matter © 2007 Elsevier Ltd. All rights reserved.
doi:10.1016/j.jsg.2007.06.006

transtensional and transpressional regimes. This was achieved by deriving analytical expressions for object orientations over time and plotting solutions for a variety of initial orientations.

In this paper, the theoretical distribution of rigid object populations as a function of both axial ratio and deformation regime is derived for a general 2D deformation. A method is suggested which allows for estimation of the finite strain and kinematics of the responsible deformation. It is important to acknowledge the limitations of the approach at the outset which are directly related to the mathematical models utilised. Firstly, the method derived is valid only for the 2D case, and in contrast to typical R_f/ϕ methods, 3D effects may be important in practice. In other words, identical 2D elliptical sections through differently shaped ellipsoids will behave differently. Secondly, inherent in Jeffery's (1922) model for rigid particle motion, the particle is isolated and interaction effects are not taken into consideration. Interaction is likely to be an important component of natural behaviour of particle populations.

2. Flow kinematics, rigid object rotation and finite strain evolution

The modelling approach of Mulchrone et al. (2005) is closely followed and many of the details are therefore omitted. Important equations are listed and some derivations regarding the finite strain state are presented. Homogeneous flows described by the velocity gradient tensor:

$$\mathbf{L} = \begin{pmatrix} 0 & L_{12} \\ L_{21} & 0 \end{pmatrix} \tag{1}$$

are considered. This flow is automatically incompressible and admits all general deformations recognised by Ramberg (1975), Means et al. (1980) and Ghosh (1987) and the kinematic vorticity number is given by:

$$W_k = \frac{L_{12} - L_{21}}{|L_{12} + L_{21}|} \tag{2}$$

The convention for angles and rotations used here is that the positive ordinate axis is the zero angle direction and the counter-clockwise angles and rotations are positive and vice versa for the clockwise case.

The eigenvectors of $\mathbf{L}$ (also known as the flow apophyses by Ramberg, 1975) are directions of zero rotation, i.e. material particles initially within these directions remain so, whereas other particles tend to be repelled from or asymptotically attracted into the flow apophyses (Passchier, 1997). They are particularly helpful in visualising the passive behaviour of points and lines as they divide the flow into zones of counter-clockwise and clockwise rotation (see Fig. 1). Taking $\xi = \sqrt{L_{12}/L_{21}}$, the eigenvectors are given by:

$$l_1 = \begin{pmatrix} \xi \\ 1 \end{pmatrix} \text{ and } l_2 = \begin{pmatrix} -\xi \\ 1 \end{pmatrix} \tag{3}$$

and have orientations:

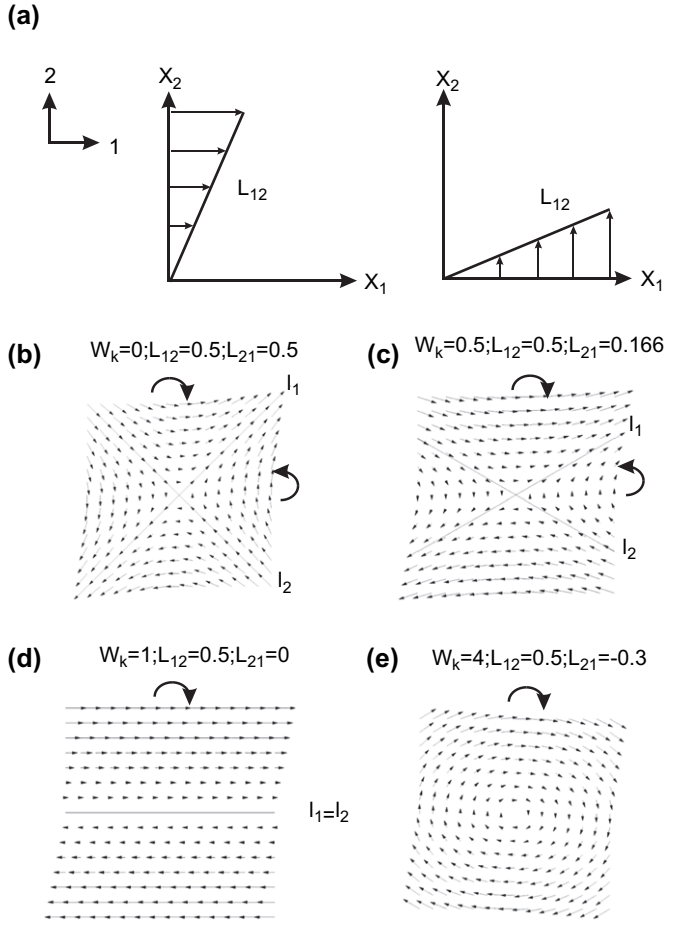

Fig. 1. (a) Velocity gradient tensor components L_{12} and L_{21} describe how the velocity vectors (small arrows) linearly vary near the origin. Combining these components in different proportions generates all possible flow types. For example, (b) $W_k = 0$, pure shear with two mutually normal flow apophyses (l_1 and l_2). Heavy arrows show the local rotation sense. (c) $W_k = 0.5$, intermediate between pure and simple shear, with two sub-normal flow apophyses. (d) $W_k = 1$, simple shear both flow apophyses coincide along the shear direction and (e) $W_k = 4$, no real apophyses exist and pulsating strain histories occur.

$$\theta_1 = \tan^{-1}\left(\frac{1}{\xi}\right) \text{ and } \theta_2 = -\tan^{-1}\left(\frac{1}{\xi}\right)$$

It is clear that for $|W_k| > 1$, some of the components of the eigenvectors are imaginary and do not have a physical meaning. The two eigenvectors coincide under simple shear ($|W_k| = 1$) and in all other cases remain distinct.

Under a general deformation of the type described by Eq. (1), Mulchrone et al. (2005) have shown that a rigid elliptical object rotates at a rate given by:

$$\dot{\phi} = \frac{L_{21} - L_{12}}{2} + \frac{(L_{21} + L_{12})(R^2 - 1)}{2(R^2 + 1)} \cos 2\phi \tag{4}$$

where ϕ is the orientation of the major axis of the object and R is the axial ratio. This equation is used extensively in the next section.

As one of the aims of this paper is to explore the relationship between rigid object fabrics and the strain ellipse, equations are derived that describe the evolution of the strain

ellipse during the general deformation. The motion of a point p initially at (x_{10}, x_{20}) is obtained by solving the following system of ordinary differential equations:

$$\frac{dx_1}{dt} = L_{12}x_2 \text{ and } \frac{dx_2}{dt} = L_{21}x_1 \tag{5}$$

with the solution:

$$x_1(t) = x_{10}\cosh(\omega t) + x_{20}\xi \sinh(\omega t) \tag{6}$$

$$x_2(t) = \frac{x_{10}}{\xi}\sinh(\omega t) + x_{20}\cosh(\omega t) \tag{7}$$

where $\omega = \sqrt{L_{12}L_{21}}$. If $L_{12}L_{21} < 0$ (i.e. different signs) then periodic solutions are possible, however, the following identities $\cosh(ix) = \cos(x)$ and $\sinh(ix) = i\sin(x)$ take care of any modifications required. This also implies that periodic solutions are only possible for $W_k < -1$ or $W_k > 1$. In the case where either of L_{12} or L_{21} takes the value 0, we have the following limiting cases: for $L_{12} = 0$:

$$x_1(t) = x_{10} \tag{8}$$

$$x_2(t) = x_{10}L_{21}t + x_{20} \tag{9}$$

and for $L_{21} = 0$:

$$x_1(t) = x_{10} + x_{20}L_{12}t \tag{10}$$

$$x_2(t) = x_{20} \tag{11}$$

which correspond to simple shear parallel to the x_2 and x_1 directions, respectively.

In order to derive information about the finite strain ellipse the approach of Ramsay (1967, p. 58) is taken. Eqs. (6) and (7) are solved for x_{10} and x_{20} and then substituted into the equation of the unit circle, i.e. $x_{10}^2 + x_{20}^2 - 1 = 0$ to give the equation of strain ellipse:

$$Ax_1^2 + Bx_2^2 + Cx_1x_2 - 1 = 0 \tag{12}$$

where:

$$A = \cosh^2(\omega t) + 1/\xi^2 \sinh^2(\omega t); \quad B = \cosh^2(\omega t) + \xi^2 \sinh^2(\omega t); \quad C = -\frac{1+\xi^2}{\xi}\sinh(2\omega t) \tag{13}$$

From coordinate geometry (Sommerville, 1949, p. 126–128) the major (or minor) axis orientation (ϕ_s) and axial ratio (R_s) (or inverted axial ratio) of the strain ellipse are given by:

$$\phi_s = \frac{1}{2}\tan^{-1}\left(\frac{C}{A-B}\right) = \frac{1}{2}\tan^{-1}\left(\frac{2\xi\coth(\omega t)}{\xi^2-1}\right) \tag{14}$$

$$R_s = \sqrt{\frac{A+B+\sqrt{(A-B)^2+C^2}}{A+B-\sqrt{(A-B)^2+C^2}}} \tag{15}$$

$$= \sqrt{\frac{1+\xi^4+2\xi^2\coth 2\omega t + (1+\xi^2)\sqrt{(\xi^2-1)^2+4\xi^2\coth^2(\omega t)}}{1+\xi^4+2\xi^2\coth 2\omega t - (1+\xi^2)\sqrt{(\xi^2-1)^2+4\xi^2\coth^2(\omega t)}}} \tag{16}$$

If $R_s < 1$, then it should be inverted and the value of ϕ_s should be modified by adding or subtracting $\pi/2$. This is because Eq. (14) may, for certain parameter values, identify the minor axis instead of the major axis. After much algebraic manipulation it can be shown that the relationship between time t and finite strain R_s is:

$$t = \frac{1}{\omega}\sinh^{-1}\left[\sqrt{\frac{\sqrt{\xi^4(1+\xi^2)^4R_s^2(1+R_s^2)^2} - 2R_s^2(\xi+\xi^3)^2}{(1+\xi^2)^4R_s^2}}\right] \tag{17}$$

and in the limit as $L_{21} \to 0$ (i.e. if $L_{12} \neq 0$, this is simple shear) then:

$$t = \frac{1}{\sqrt{L_{12}}}\sqrt{\frac{\sqrt{L_{12}^6(R_s+R_s^3)^2} - 2L_{12}^3R_s^2}{L_{12}^4R_s^2}}$$

These expressions come in very handy when plotting various expressions as a function of finite strain as opposed to the geologically meaningless (at least usually) time parameter. It is worth noting that for $|W_k| > 1$, i.e. pulsating deformation histories, the relationship between R_s and t becomes non-unique, in which case evaluating the evolution of the system by time is more reliable.

By solving Eq. (14) for time, substituting into Eq. (16), and taking account of Eq. (7), an expression relating ϕ_s, R_s and W_k is derived:

$$R_s = \sqrt{\frac{1+2W_k\sqrt{\sec^2(2\phi_s)} + W_k^2(1+\tan^2(2\phi_s))}{1-2W_k\sqrt{\sec^2(2\phi_s)} + W_k^2(1+\tan^2(2\phi_s))}} \tag{18}$$

this equation needs to be inverted for $W_k < 0$ but can be used as given for $W_k > 0$. Similar relationships have been derived previously by Tikoff and Fossen (1995) and suggested as a practical method for estimating W_k. Recently, Czeck and Hudleston (2003) have successfully applied this type of analysis to conglomerates in the Archean Superior Province in the North America craton. Eq. (18) can be used to derive an expression for ϕ_s in terms of R_s and W_k, and W_k in terms of ϕ_s and R_s:

$$\phi_s = \frac{1}{2}\sec^{-1}\left(\frac{R_s+1}{W_k(R_s-1)}\right) \tag{19}$$

$$W_k = \frac{\cos^2(2\phi_s)\left(\left(R_s^2+1\right)\sqrt{\sec^2(2\phi_s)} \pm 2\sqrt{R_s^2\sec^2(2\phi_s)}\right)}{R_s - 1} \tag{20}$$

Notice that there are two solutions for W_k, one giving $|W_k| \leq 1$, i.e. pure to simple shear and another for $|W_k| > 1$, i.e. super shear or pulsating deformation histories. These equations encapsulate the idea that under different deformation conditions, a particular relationship between the intensity and orientation of the finite strain ellipse exists. In a region, where deformation conditions were spatially uniform, but resulted in different levels of finite strain due to spatially varying deformation rates, then the variation in R_s versus ϕ_s could be used to estimate the value of W_k (Tikoff and Fossen, 1995; Czeck and Hudleston, 2003).

3. Fabrics due to a population of rigid objects undergoing a general deformation

3.1. Introduction

In this section, the probability density function (pdf) to describe the fabric developed by a population of rigid elliptical objects under a general deformation is derived. A pdf is a function which gives the relative probability that an elliptical object is oriented with its long axis along a particular direction. For circular data, pdfs have the following properties (Mardia, 1972, p. 40):

1. $f(\phi) \geq 0, \quad -\infty < \phi < \infty$
2. $f(\phi + 2\pi) = f(\phi), \quad -\infty < \phi < \infty$
3. $\int_0^{2\pi} f(\phi)\mathrm{d}\phi = 1$

where ϕ is long axis orientation in radians and f is the pdf. The probability P that the orientation of an object lies between two orientations (ϕ_1 and ϕ_2) is given by:

$$P = \int_{\phi_1}^{\phi_2} f(\phi)\mathrm{d}\phi \tag{21}$$

For every pdf there is a corresponding distribution function (F) defined as (Mardia, 1972, p. 39; Allen, 1978, p. 81):

$$\frac{\mathrm{d}F}{\mathrm{d}\phi} = f(\phi) \tag{22}$$

$$f(\phi) = \frac{1}{2\pi}, \quad -\infty < \phi < \infty \tag{23}$$

3.2. Probability density function

The rotation rate of a single rigid object under a general deformation, as described in the previous section, is given by Eq. (8) which may be written as:

$$\dot{\phi} = \alpha + \beta\cos 2\phi \tag{24}$$

where $\alpha = (L_{21} - L_{12})/2$ and $\beta = ((L_{21} + L_{12})(R^2 - 1))/2(R^2 + 1)$. The solution to this differential equation is given by:

$$\phi(t) = -\tan^{-1}\frac{\sqrt{\beta^2-\alpha^2}\tanh\left(\sqrt{\beta^2-\alpha^2}t + \tanh^{-1}\left(\frac{\sqrt{\beta^2-\alpha^2}\tan\phi_0}{\alpha+\beta}\right)\right)}{\alpha-\beta} \tag{25}$$

where ϕ_0 is the initial orientation of the ellipse long axis. So that given the deformation regime, object aspect ratio and initial orientation, we can determine orientation at any time in the future.

However, from elementary calculus (Mulchrone, 2002):

$$\frac{\mathrm{d}F}{\mathrm{d}\phi} = \frac{\mathrm{d}F}{\mathrm{d}\phi_0}\frac{\mathrm{d}\phi_0}{\mathrm{d}\phi} \tag{26}$$

that is:

$$f(\phi) = f(\phi_0)\frac{\mathrm{d}\phi_0}{\mathrm{d}\phi} \tag{27}$$

In other words, the pdf at any time t is the product of the initial form of the pdf and the derivative $(\mathrm{d}\phi_0/\mathrm{d}\phi)$. The pdf for a population of rigid objects can now be derived, if it is assumed that the long axes were initially uniformly distributed. From Eq. (25):

$$\phi_0 = \tan^{-1}\left[\frac{\sqrt{\beta^2-\alpha^2}\tanh\left(\sqrt{\beta^2-\alpha^2}t - \tanh^{-1}\left(\frac{\sqrt{\beta^2-\alpha^2}\tan\phi}{\alpha+\beta}\right)\right)}{\alpha-\beta}\right] \tag{28}$$

Differentiating Eq. (28) and substituting the result and Eq. (23) into Eq. (27) gives the pdf for a deformed initially uniform distribution of rigid ellipses:

$$f(\phi) = \frac{(\alpha-\beta)(\alpha+\beta)}{2\pi(\alpha+\beta\cos 2\phi)\left(\alpha - \beta\cosh\left[2\sqrt{\beta^2-\alpha^2}t - 2\tanh^{-1}\left(\frac{\sqrt{\beta^2-\alpha^2}\tan\phi}{\alpha+\beta}\right)\right]\right)} \tag{29}$$

The pdf of a uniform distribution of objects is given by (Mardia, 1972, p. 50):

There are two varieties of solution, stable and periodic, when considering the evolution of this pdf over time. This

result is derived by considering the form of the cosh term under the line, which is the only time dependent term. The value of $\sqrt{\beta^2-\alpha^2}$ can be either real or imaginary depending on the values of α and β, i.e. L_{12}, L_{21} and R. If $\sqrt{\beta^2-\alpha^2}$ is real then the cosh term keeps the form shown in Eq. (29) and the solution is non-periodic and the pdf becomes more and more intense as time progresses. If $\sqrt{\beta^2-\alpha^2}$ is imaginary then, by noting that $\tanh^{-1}(\mathrm{i}x) = \mathrm{i}\tan^{-1}(x)$ and $\cosh(\mathrm{i}x) = \cos(x)$, the solution becomes:

$$f(\phi) = \frac{(\alpha-\beta)(\alpha+\beta)}{2\pi(\alpha+\beta\cos 2\phi)\left(\alpha-\beta\cos\left[2\sqrt{\alpha^2-\beta^2}t - 2\tan^{-1}\left(\frac{\sqrt{\alpha^2-\beta^2}\tan\phi}{\alpha+\beta}\right)\right]\right)} \tag{30}$$

In this case the pdf evolves in periodically over time due to the cos term, becoming successively more and less intense. The term $\sqrt{\beta^2-\alpha^2}$ is real if:

$$\beta^2 > \alpha^2 \tag{31}$$

which after much manipulation amounts to stable solutions for:

$$-\frac{R^2-1}{R^2+1} < W_k < \frac{R^2-1}{R^2+1} \tag{32}$$

and periodic solutions otherwise. This is exactly the same criteria which distinguishes between continuously and asymptotically rotating individual objects (Mulchrone et al., 2005). The period of the fabric cycle is given by:

$$\frac{\pi}{\sqrt{\alpha^2-\beta^2}} = \frac{2\pi}{\sqrt{(L_{12}+L_{21})^2}\sqrt{W_k^2-\left(\frac{R^2-1}{R^2+1}\right)^2}} \tag{33}$$

so that larger W_k results in shorter fabric cycles whereas larger R results in longer cycles.

3.3. Behaviour of the probability density function

In this section, the properties of the pdf in Eq. (29) are graphically investigated. Consistent with the analysis of the previous section, Fig. 2(a) and (b) plainly illustrate the different population behaviours under simple and pure shear. In simple shear the clustering of orientation becomes periodically more and less dense, whereas under pure shear it always becomes more intense. Looking instead at the behaviour of aspect ratios between 1 and 10 it is clear that for low finite strain (i.e. Fig. 2(c) and (d)) there is little difference between the populations under simple and pure shear. This similarity will be echoed in both the statistical parameters' study and parameter estimation technique introduced below. However, as the finite strain increases obvious differences emerge. Comparing Fig. 2(e) with (f) ($R_s = 20.0$) and Fig. 2(g) with (h) ($R_s = 60.0$) the rotational aspect of populations becomes apparent, i.e. under simple shear a general asymmetry appears. Also at the highest strain levels (Fig. 2(g)) the pulsating fabric effect seen in Fig. 2(a) kicks in and the fabric of the lower aspect ratio section of the population begins to become less intense. This cannot occur under pure shear.

3.4. Statistics for describing rigid object populations

In studying the intensity and mean orientation of a shape fabric of populations of rigid elliptical objects, it is desirable to choose measures which can be applied to natural data. This facilitates the development of methods based on theory which can be applied in practice. It is proposed here that the mean resultant length ($\overline{R}_1$), mean orientation ($\overline{\phi}_1$), skewness (s) or asymmetry and kurtosis (k) or peakedness commonly used in circular statistics (Mardia, 1972, p. 20, 34–35; Fisher, 1993, p. 31–34) be used to represent the intensity, orientation, symmetry and form of a shape fabric, respectively. $\overline{R}(=\overline{R}_1)$ has already been used by Mulchrone (2002) and has been directly related to the strain ellipse for populations of passively deformed linear elements. Masuda et al. (1999) used a von Mises distribution to characterise fabrics, which entailed calculating $\overline{R}$ and $\overline{\phi}_1$. In this section a bar denotes a quantity evaluated using discrete data, whereas the absence of a bar indicates a quantity evaluated theoretically. For a discrete set of n ellipse orientations, we calculate:

$$\overline{S}_p = \frac{1}{n}\sum_{i=1}^{n}\sin p\phi_i \tag{34}$$

$$\overline{C}_p = \frac{1}{n}\sum_{i=1}^{n}\cos p\phi_i \tag{35}$$

then the mean resultant length and orientation are:

$$\overline{R}_p = \frac{1}{n}\sqrt{\overline{S}_p^2+\overline{C}_p^2} \tag{36}$$

$$\overline{\phi}_p = \tan^{-1}\left(\frac{\overline{S}_p}{\overline{C}_p}\right) \tag{37}$$

Normally $\overline{R}_1$ is simply denoted by $\overline{R}$ and $\overline{\phi}_1$ by $\overline{\phi}$. An estimate for $\overline{R}_1$ derived from a population is denoted by $\widehat{\rho}_1$ and likewise $\overline{\phi}_1$ is estimated by $\widehat{\mu}_1$. In general a 'hat' denotes a population estimate. Kurtosis and skewness measures are normally derived using the centered trigonometric moments as follows:

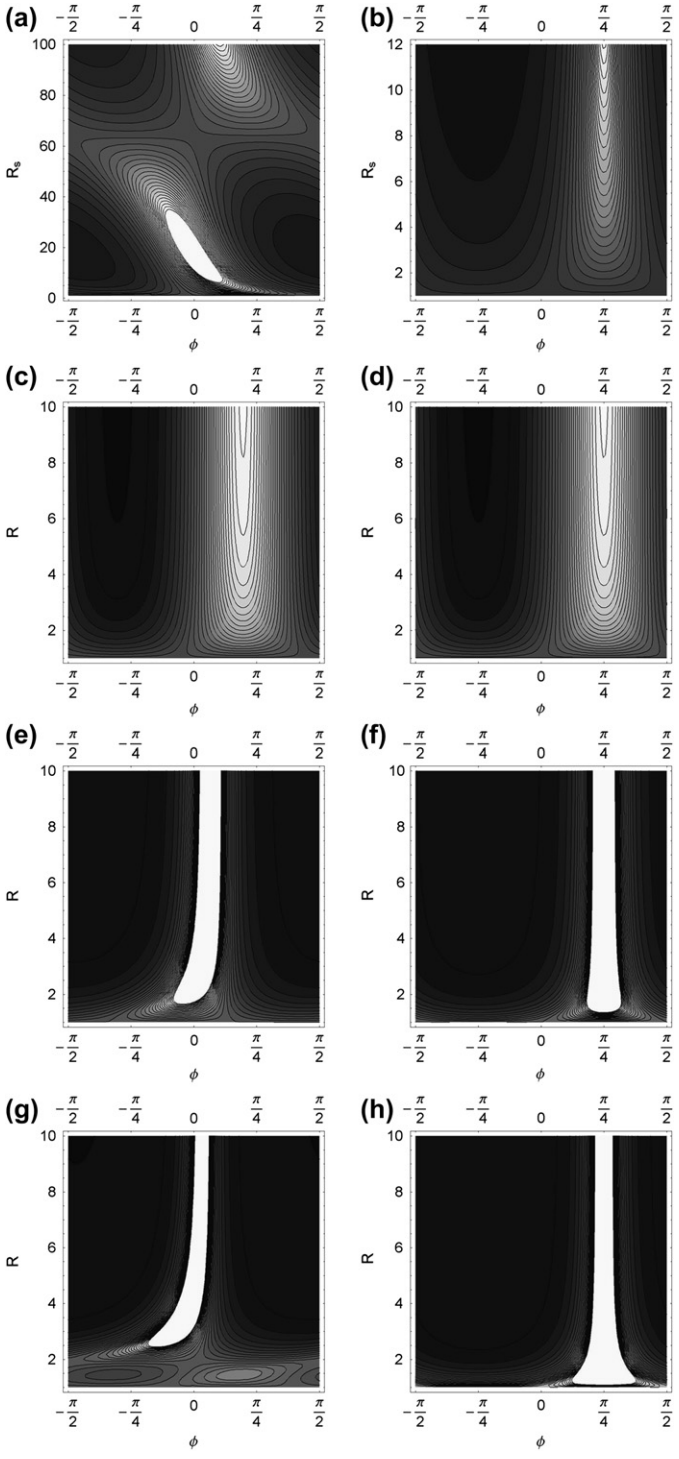

Fig. 2. Contour plots of theoretical pdf for populations of rigid objects. Lighter areas represent higher probabilities whereas the reverse applies for darker regions. (a) Simple shear for object aspect ratio $R = 2.0$. (b) Pure shear for object aspect ratio $R = 2.0$. (c) Simple shear, $R_s = 2.0$. (d) Pure shear, $R_s = 2.0$. (e) Simple shear, $R_s = 20.0$. (f) Pure shear, $R_s = 20.0$. (g) Simple shear, $R_s = 60.0$. (h) Pure shear, $R_s = 60.0$.

$$\overline{S}'_p = \frac{1}{n}\sum_{i=1}^{n} \sin p(\phi_i - \overline{\phi}_1)$$
$$\overline{C}'_p = \frac{1}{n}\sum_{i=1}^{n} \cos p(\phi_i - \overline{\phi}_1)$$

which give corresponding measures $\overline{R}'_1$ and $\overline{\phi}'_p$. Then kurtosis and skewness can be defined (Fisher, 1993, p. 34):

$$\overline{s} = \frac{\overline{R}'_2 \sin\left(\overline{\phi}'_2 - 2\overline{\phi}'_1\right)}{\left(1 - R'_1\right)^{3/2}} \tag{38}$$

$$\overline{k} = \frac{\overline{R}'_2 \cos\left(\overline{\phi}'_2 - 2\overline{\phi}'_1\right) - \overline{R}'^4_1}{\left(1 - \overline{R}'_1\right)^2} \tag{39}$$

Ellipse orientation data are axial, i.e. $\phi_i = \phi_i \pm j\pi$, where j is an integer, and results in the cross-over problem (Fisher, 1993, p. 31). To avoid this problem the data are first doubled prior to application of Eq. (34)–(39), and therefore to retrieve the correct mean orientation the result of Eq. (37) should be halved.

The continuous analogues of Eqs. (34) and (35) are given by (Mulchrone, 2002):

$$S_p = \int_0^{2\pi} \sin(p\phi) f(\phi/2) \mathrm{d}\phi \tag{40}$$

$$C_p = \int_0^{2\pi} \sin(p\phi) f(\phi/2) \mathrm{d}\phi \tag{41}$$

with the centered trigonometric moments given by (Fisher, 1993, p. 41):

$$S'_p = \int_0^{2\pi} \sin(p(\phi - \phi_1)) f(\phi/2) \mathrm{d}\phi \tag{42}$$

$$C'_p = \int_0^{2\pi} \sin(p(\phi - \phi_1)) f(\phi/2) \mathrm{d}\phi \tag{43}$$

where f is the pdf and the argument to the pdf is halved to take account of the cross-over problem (i.e. halving the argument doubles the wavelength). This implies that the output from Eq. (37) also needs to be halved to give the correct mean orientation. In order to calculate the parameters (R_1, ϕ_1, s and k) for the theoretical pdf, Eqs. (40)–(43) need to be evaluated for $p = 1$ and 2. The continuous versions of the expressions for skewness and kurtosis are (Fisher, 1993, p. 42):

$$s = \frac{S'_2}{\left(1 - R'_1\right)^{3/2}}$$

$$k = \frac{C'_2 - R'^4_1}{\left(1 - R'_1\right)^2}$$

Eq. (29) can be rewritten in the following form:

$$f(\phi) = \frac{a_1}{2\pi(b_1 + c_1\cos(2\phi) + d_1\sin(2\phi))} \tag{44}$$

where:

$$\begin{aligned} a_1 &= (\alpha-\beta)(\alpha+\beta), \quad b_1 = \alpha^2 - \beta^2\cosh\left(2\sqrt{\beta^2-\alpha^2}t\right) \\ c_1 &= -2\alpha\beta\sinh^2\left(2\sqrt{\beta^2-\alpha^2}t\right), \quad d_1 = \beta\sqrt{\beta^2-\alpha^2}\sinh\left(2\sqrt{\beta^2-\alpha^2}t\right) \end{aligned} \tag{45}$$

This transformation facilitates evaluation of the integrals required in Eqs. (40) and (41), which turn out to have analytical solutions. Key solutions are written out in the Appendix. It is noteworthy that $S_2' = 0$, which implies that skewness is expected to be close to 0 and that symmetric distributions occur independent of the type of deformation. Additionally $S_2' = 0$, which implies that $\phi_1' = 0$ for centered distributions (this is to be expected since the distributions have been re-oriented by the mean orientation ϕ_1 see Eqs. (42) and (43).

3.5. Behaviour of rigid object population statistics during deformation

One possible method of estimating both the finite strain and type of deformation that lead to a particular distribution is to examine the theoretical behaviour of the above statistical parameters. Fig. 3 illustrates the relationship between the centered mean resultant vector (R_1') and finite strain and W_k. For populations of objects with low aspect ratio R_1' tends to vary quite markedly with W_k and R_s. Therefore R_1' is difficult to interpret in such cases (see Fig. 3(a) and (b)). However, by considering the high aspect ratio population, i.e. $R > 5$ then the variation with W_k diminishes enabling a good estimate of R_s to be found (see Fig. 3(d)). This result immediately suggests a graphical technique for rigid object population analysis whereby high aspect ratio objects are used to estimate R_s from R_1' (i.e. Fig. 3(d) and for real data use the corresponding discrete statistic). Using the estimate of R_s, W_k can be estimated from the low aspect ratio subpopulation (i.e. Fig. 3(a)). It is interesting to note that even for $R = 1.5$ (Fig. 3(a)), the curves for different values of W_k are indistinguishable for low finite strains. Additionally, even at high finite strains the curves for $0.0 \le W_k \le 0.66$ are extremely close together, which implies that the quality and quantity of data required to differentiate between these possibilities may

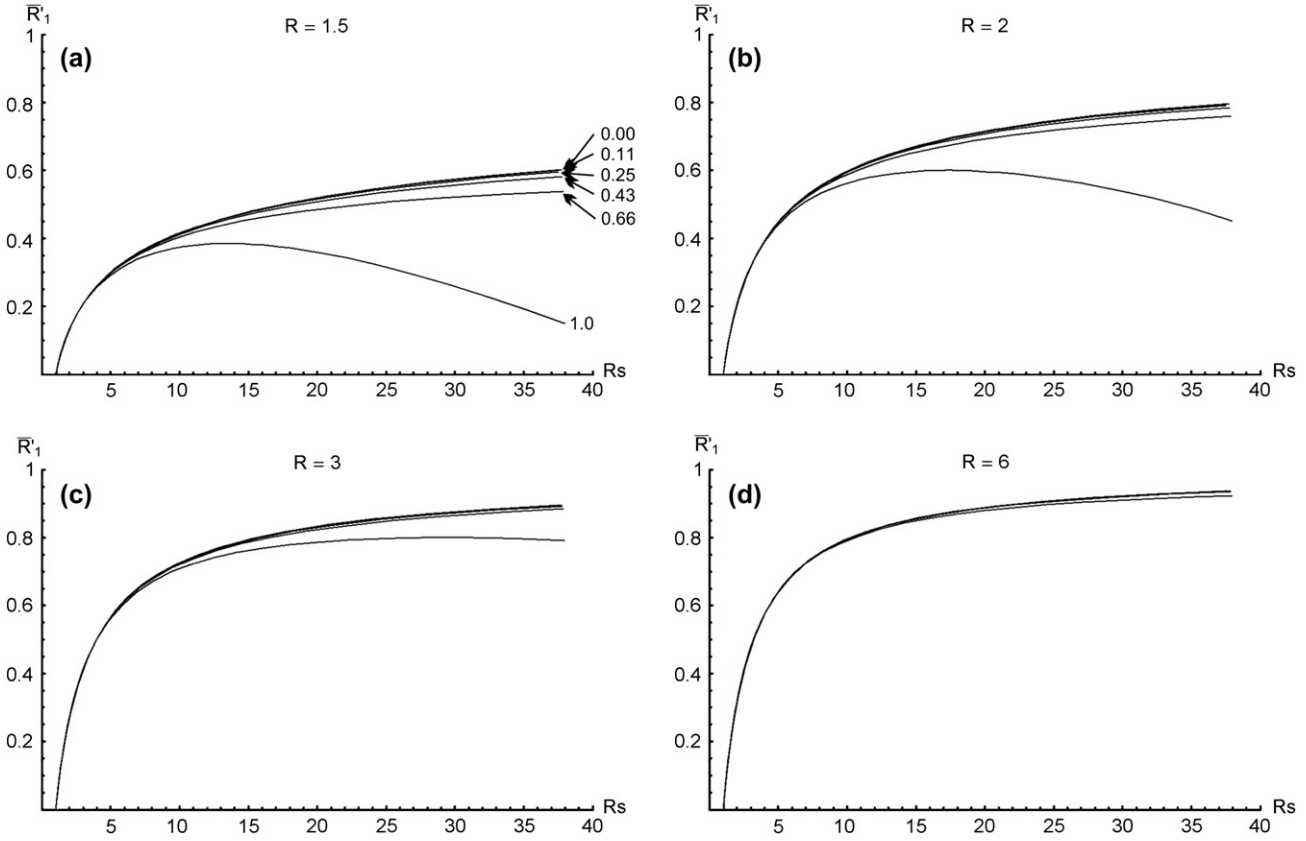

Fig. 3. Plot of theoretical centered mean resultant vector (R_1') versus finite strain for various object axial ratios and flow types. The numbers on (a) are kinematic vorticity numbers (W_k). The plots in (b)–(d) show a similar trend, i.e. the lowest curve is for $W_k = 1$ and lower values occur for the higher and less distinguishable curves.

not be readily available in the field, keeping in mind that every estimate for R'_1 will incorporate some sampling error at the very minimum.

An alternative approach involves comparing the mean orientations (i.e. ϕ_1) of subpopulations segregated by aspect ratio. Let the mean orientation of a subpopulation with aspect ratio R be denoted by $\phi_1^{(R)}$. In the field it is usually difficult to accurately identify the kinematic reference frame of a deformation without first making assumptions about the nature of the deformation (which defeats the purpose of trying to independently estimate W_k). Therefore in the absence of a readily identifiable reference frame it makes sense to compare the difference in orientation between two subpopulations. Let $\phi_1^{(R_a,R_b)} = \phi_1^{(R_a)} - \phi_1^{(R_b)}$. The relationship between $\phi_1^{(R_a,R_b)}$, W_k and R_s is investigated in Fig. 4. These plots indicate the importance of both W_k and R_s in the interpretation of these angular relationships. An independent estimate of R_s is required in order to calculate a value for W_k. However, unlike the mean resultant vector method above, comparing mean orientation cannot give an independent estimate of R_s. In general, the closer together and higher the subpopulation aspect ratios, the less distinguishable are the curves. The optimal dataset would include

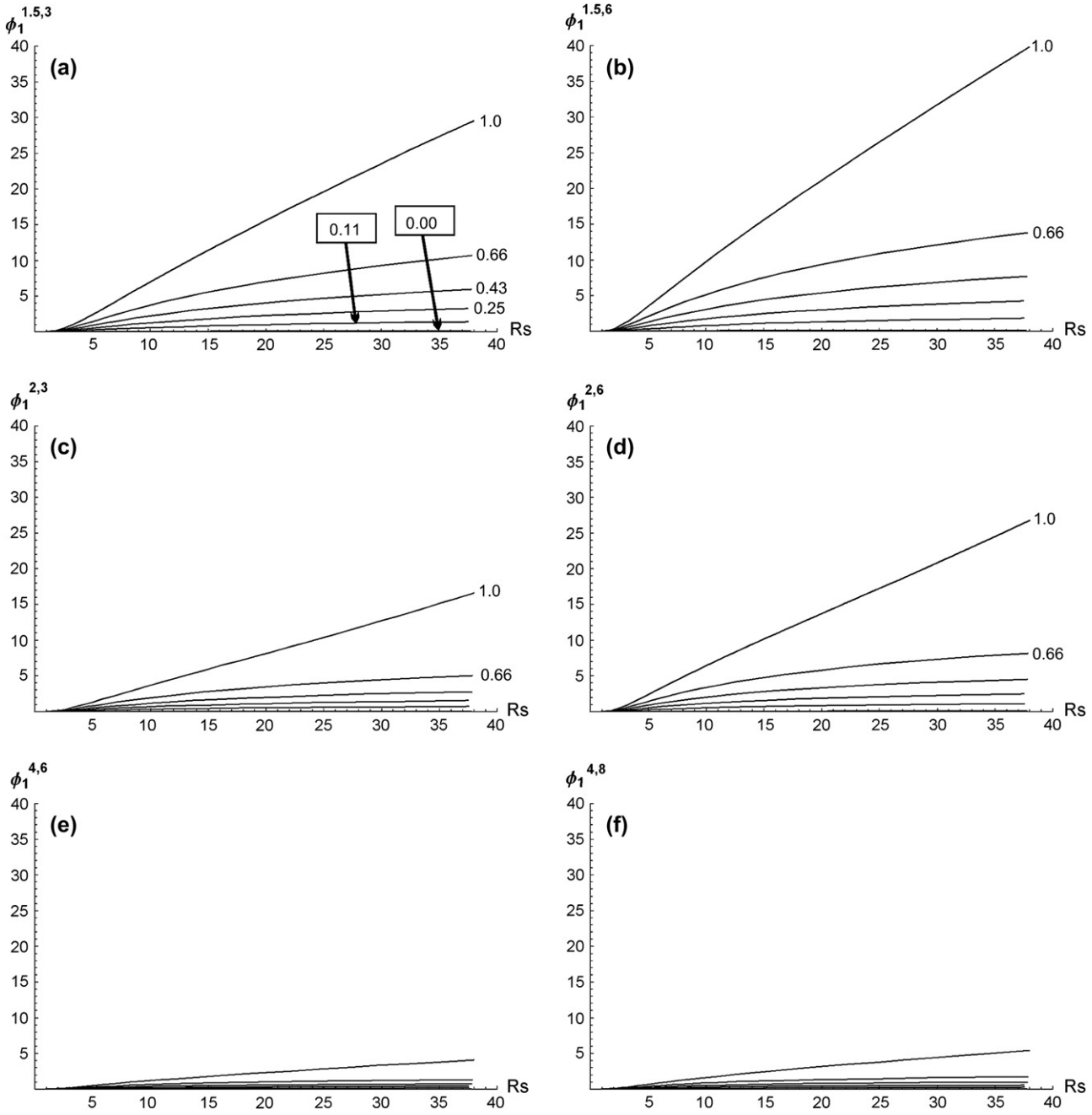

Fig. 4. Plot of theoretical mean orientation difference between two subpopulations. Numbers annotated on curves give values for W_k. For the sake of legibility not all curves are labeled in (b)–(d), but the pattern is similar to that found in (a). (a) Mean orientation difference between subpopulations ($R = 1.5$ and 3.0); (b) $R = 1.5$ and 6.0; (c) $R = 2.0$ and 3.0; (d) $R = 2.0$ and 6.0; (e) $R = 4.0$ and 6.0; (f) $R = 4.0$ and 8.0.

data from low aspect ratio objects and high aspect ratio objects. There are limitations associated with this type of analysis. Even if an ideal dataset were obtained (i.e. $R = 1.5$ and 6.0 as in Fig. 4(b)) then R_s should be greater than 10 in order to distinguish W_k. Consider the case of Fig. 4(b), where even at high finite strain, determining $W_k \leq 0.43$ requires the ability to accurately identify $\phi_1^{(1.5,6.0)} < 5^\circ$. Given the occurrence of sampling error in practice, the method is likely to be of low accuracy at best. It is unlikely that data of a suitable type, quality and in sufficient quantity could be collected from a natural example.

The skewness of a deformed rigid object population is theoretically predicted to be zero, however, kurtosis might be a useful parameter. The variation of kurtosis with W_k and R_s is shown for selected aspect ratios in Fig. 5. Again the pattern is similar to that seen for other statistical parameters, whereby an independent estimate of R_s is required to estimate W_k and the accuracy of estimating W_k is unlikely to be accurate for $W_k \leq 0.43$.

4. Maximum likelihood estimation of deformation parameters

4.1. Introduction

Maximum likelihood parameter estimation (MLE) is one of the most widely used estimation techniques employed by statisticians (Devore, 1995, p. 270). It can sometimes be used to derive analytical expressions for estimating parameters but importantly there is a numerically based approach which works provided the probability density function is known. Suppose that $\mathbf{x}$ is an observation (it may comprise one or more values, for example, in the present case each $\mathbf{x}$ would be made up of a pair of object axial ratio, R_i, and long axis orientation, ϕ_i values) and $\boldsymbol{\theta}$ is a set of one or more parameters and the pdf is given by $f(\mathbf{x}, \boldsymbol{\theta})$. Then the likelihood function is defined as:

$$L(\mathbf{x}_1, \mathbf{x}_2, \ldots, \mathbf{x}_n, \boldsymbol{\theta}) = \prod_{i=1}^{n} f(\mathbf{x}_i, \boldsymbol{\theta}) \tag{46}$$

The maximum likelihood estimation of the parameters $\boldsymbol{\theta}$, is the value $\frown\boldsymbol{\theta}$ which maximises L. It is equivalent and often practically easier and more efficient to maximise the natural log of L. In seeking analytical solutions, calculus is employed to estimate $\frown\boldsymbol{\theta}$ by looking at the derivatives of L with respect to the parameters. In the present case (see Eqs. (30) and (20)), this approach becomes intractable and therefore a numerical approach is favoured.

In a natural sample, we can measure $\mathbf{x}_i = (R_i, \phi_i)$ for a population of n objects. Consulting the pdf derived earlier (see Eq. (29)) and noting the interchangeability of time t and R_s, our unknown set of parameters is $\boldsymbol{\theta} = (L_{12}, L_{21}, R_s, \phi_{ref})$. In the case of natural data the reference direction for orientation measurement may not parallel the orientation of the kinematic reference frame (chosen here for convenience so that the velocity gradient tensor takes the form shown in Eq. (1)). Therefore each ϕ_i is modified to $\phi_i - \phi_{ref}$ so that this potential discrepancy can be handled. The parameter list can be condensed further by considering the expression for W_k (see Eq. (2)). Divide above and below by L_{21} to get:

$$W_k = \frac{\frac{L_{12}}{L_{21}} - 1}{\left|\frac{L_{12}}{L_{21}} + 1\right|}$$

implying that W_k depends on the ratio rather than the absolute values of L_{12} and L_{21}. Therefore without any loss of generality L_{12} can be assigned the value 1 and then our parameter list

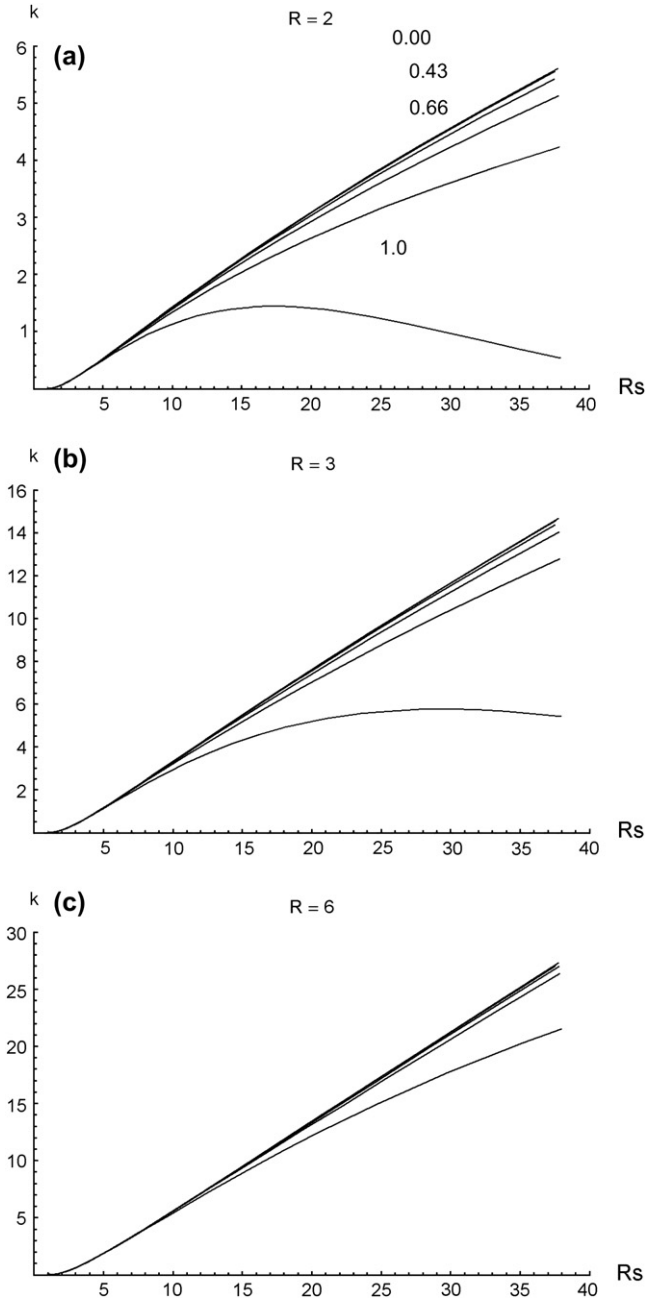

Fig. 5. Plot of kurtosis (k) versus R_s for populations with aspect ratios of (a) 2.0; (b) 3.0; and (c) 6.0. Numbers annotated in (a) are for W_k and (b) and (c) follow a similar pattern. Notice the varying ordinate axis scales.

becomes $\boldsymbol{\theta} = (L_{21}, R_s, \phi_{ref})$ so that W_k can be determined from the estimate of L_{21}.

Using the pdf for a rigid object population (Eq. (29)) derived earlier the likelihood function is constructed as follows. For each data point $\mathbf{x}_i$ substitute the values of R_i, ϕ_i into Eq. (29) in place of R and ϕ. Additionally let L_{12} take the value 1 and substitute in the value of t from Eq. (17). Finally take the natural log of the expression and sum over all $\mathbf{x}_i$. Numerical methods, readily available in software packages such as Mathematica and Matlab, can be used to find the parameter values (i.e. L_{21}, R_s and ϕ_{ref}) which maximise the likelihood function.

4.2. Simulation

In order to test the new method for finite strain estimation and vorticity analysis, a simulation experiment was carried out to assess the performance of the method under ideal conditions (i.e. the only source of error is from the sampling distribution). This turned out to be a very useful exercise because even though the method nearly always accurately calculates finite strain, there are significant limitations on its ability to estimate W_k in line with the earlier more qualitative analysis. Therefore this simulation provides a partial guide to the proper use of the method in practice.

Results are presented in Figs. 6 and 7. Firstly for a large number of readings (i.e. 1000) we see that the finite strain is well estimated by the method at low applied finite strains (<40, see Fig. 6(a)). In contrast the error associated with this method of estimation increases in the case of higher applied finite strain (as evidenced from the variability of values around the true value in Fig. 6(c). This is to be expected given the increasing error behaviour with applied finite strain already documented for R_f/ϕ type methods (Meere and Mulchrone, 2003). This behaviour contrasts sharply with the method's ability to estimate W_k where the reverse situation prevails, i.e. error prone estimates at low finite strains but improved estimates at higher strains. In Fig. 7 the same set of experiments was performed but for a lower number objects ($n = 100$). A similar pattern emerges although the overall variability of the results is higher.

Under simple shear deformation cyclical population behaviour (i.e. periodically increasing and decreasing strains) is expected for a particular axial ratio and the period of the cycle depends on the axial ratio (Eq. (33)). In the simulation a range of axial ratio values was considered and for the range of R_s examined cyclical behaviour for the total population was not observed. In natural shear zones, where large movements have taken place, such cyclical population behaviour may occur. In such cases, the estimate of finite strain derived using this method may not be representative of the total finite strain. However, we can explore this concern from a theoretical perspective as well. From above, the theoretical expression for the mean orientation of a rigid object population under simple shear (i.e. $L_{21} = 0$) is given by:

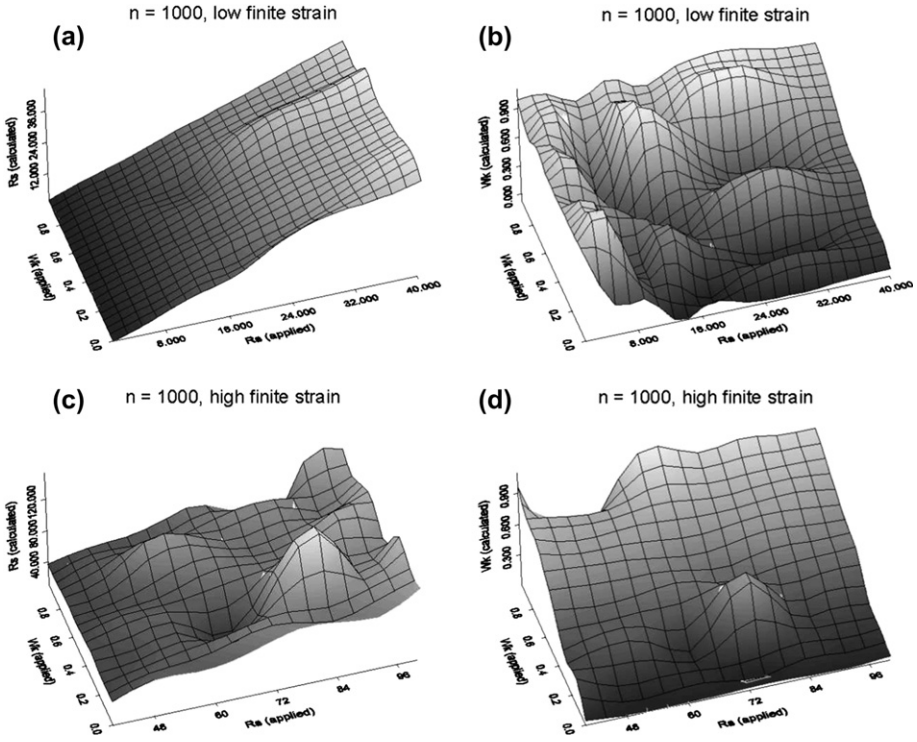

Fig. 6. Results of simulation for 1000 objects under low and high finite strain and various flow types. (a) R_s (applied) varies from 1 to 40 along the ordinate axis, W_k (applied) varies from 0 to 1 along the coordinate axis and R_s (calculated) varies along the vertical axis. The surface is relatively smooth and R_s (calculated) corresponds well with R_s (applied) independently of W_k (applied). (b) R_s (applied) varies from 1 to 40 along the ordinate axis, W_k (applied) varies from 0 to 1 along the coordinate axis and W_k (calculated) varies along the vertical axis. The surface is relatively uneven and W_k (calculated) is not always consistent with W_k (applied) except when R_s(applied) $\gtrapprox 35$. (c) Axes same as in (a). Surface is relatively uneven, indicating poor correlation between R_s (calculated) and R_s (applied). (d) Same axes as in (b). Surface is fairly smooth indicating better correlation between W_k (calculated) and W_k (applied).

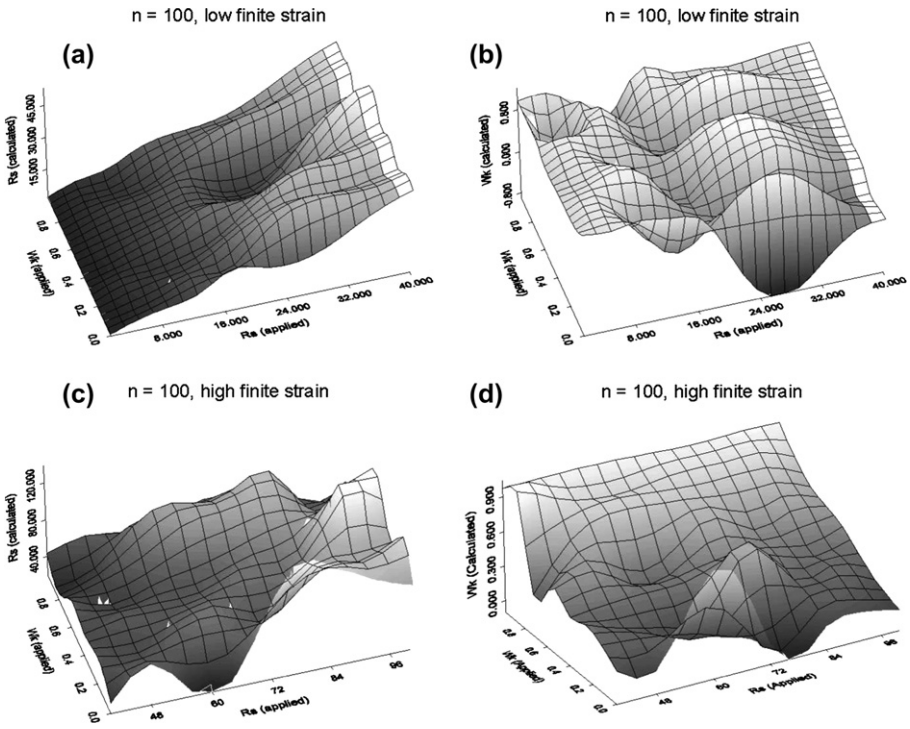

Fig. 7. Results of simulation for 100 objects under low and high finite strain and various flow types. (a) Axes as in Fig. 6(a). The surface is relatively smooth and R_s (calculated) corresponds reasonably with R_s (applied) independently of W_k (applied). (b) Axes as in Fig. 6(b). The surface is relatively uneven and W_k (calculated) is not consistent with W_k (applied) even when R_s (applied) $\gtrapprox 35$. (c) Axes as in Fig. 6(a). Surface is relatively uneven, indicating poor correlation between R_s (calculated) and R_s (applied). (d) Axes as in Fig. 6(b). Surface is fairly uneven indicating poor correlation between W_k (calculated) and W_k (applied).

$$\tan(\phi_1) = \frac{2R}{1+R^2}\cot\left(\frac{L_{12}Rt}{1+R^2}\right) \tag{47}$$

Considering a range of values of R, then for an overall periodic behaviour we expect to be able to find a period T such that:

$$\frac{2R}{1+R^2}\cot\left(\frac{L_{12}Rt}{1+R^2}\right) = \frac{2R}{1+R^2}\cot\left(\frac{L_{12}R(t+T)}{1+R^2}\right)$$

which only has a solution for $T=0$, i.e. no such period exists. Therefore, even though cyclical behaviour occurs for populations of a single axial ratio, populations exhibiting a wide range of axial ratios cannot exhibit periodicity. This means that the derived method can be used to calculate finite strain under a simple shear.

A detailed exploration of the error behaviour of the method is beyond the scope of this paper and is left for future investigation.

5. Discussion and conclusions

Extracting meaningful information from a population of elliptical objects is based on the validity of two assumptions: (i) an initially uniform distribution of long axis orientations and (ii) the mechanisms operating during deformation which bring about the modified distribution. In this paper the first assumption is retained whilst in the second assumption the usual mechanism of passive behaviour (typically made in R_f/ϕ and related methods, e.g. Ramsay, 1967, p. 202; Shimamoto and Ikeda, 1976; Robin, 1977) is replaced with that of rigid elliptical object rotation (Jeffery, 1922). There are many other possible mechanisms that may be at work (i.e. the objects may be deformable or slip may occur at the boundary or pressure solution may modify object geometries) so the method presented here is by no means the only alternative to passive behaviour. However, in cases where rigid behaviour is likely then the method developed here should provide more realistic estimates of both finite strain and vorticity number. Misapplication of the method developed here or traditional R_f/ϕ methods can lead to erroneous results, therefore blind implementation of either method is not recommended. In particular, the method derived here applies only to 2D populations where 3D effects can be ignored and it is important that the population of objects is not closely spaced such that interaction effects become important.

The ability of the method, described above, to attempt estimation of both finite strain and vorticity relates to the fact that it simultaneously utilises both axial ratio and orientation information from the population. If there is not a sufficient variation in the axial ratio distribution, then vorticity analysis is not possible. That is, for a population all with the same axial ratio, there is no difference between the shapes of the distribution of orientations under different kinematic conditions to allow the type of deformation applied to be distinguished. However, as shown above, different classes of axial ratios respond differently, relative to each other, enabling an attempt at vorticity estimation.

The probability distribution function of a population of rigid objects under a general 2D deformation and its behaviour under a variety of kinematic conditions were considered. Theoretical values for typical statistics applied to orientational data (Mardia, 1972) were also derived and may be used to graphically estimate both finite strain and vorticity. A numerical approach based on the maximum likelihood method is favoured and results of a simulation study indicate that finite strain can be nearly always accurately calculated, but that accurate estimation of W_k is only possible at high finite strains and large sample numbers.

Acknowledgements

Thoughtful and thorough reviews by Prof. Richard Lisle and Dr. F.O. Marques have greatly improved the final version of the paper. Thanks also to Prof. Tom Blenkinsop for editorial assistance and advice. This work was partially funded by the Science Foundation Ireland research frontiers program (grant 04/BR/ES0020).

A. Appendix

Letting $\kappa = \sqrt{c_1^2 + d_1^2 - b_1^2}$, the solved integrals for S_1, S_2, C_1,C_2, R_1, R_2, ϕ_1, ϕ_2, S_1', S_2', C_1' and C_2' are:

$$S_1 = \frac{a_1 d_1(\kappa + b_1 \mathrm{i})}{(c_1^2 + d_1^2)\kappa}$$

$$S_2 = \frac{2a_1 c_1 d_1\left(-2b_1\kappa + (\kappa^2 - b_1^2)\mathrm{i}\right)}{(c_1^2 + d_1^2)^2\kappa}$$

$$C_1 = \frac{a_1 c_1(\kappa + b_1 \mathrm{i})}{(c_1^2 + d_1^2)\kappa}$$

$$C_2 = \frac{a_1(c_1^2 - d_1^2)\left(-2b_1\kappa + (\kappa^2 - b_1^2)\mathrm{i}\right)}{(c_1^2 + d_1^2)^2\kappa}$$

$$R_1 = \sqrt{\frac{a_1^2\left(1 + \mathrm{i}\frac{b_1}{\kappa}\right)^2}{c_1^2 + d_1^2}}$$

$$R_2 = \sqrt{\frac{a_1^2\left(\kappa(1 + 2\mathrm{i}b_1) - b_1^2\right)}{(c_1^2 + d_1^2)^2\kappa^2}}$$

$$\phi_1 = \tan^{-1}\left(\frac{d_1}{c_1}\right)$$

$$\phi_2 = \tan^{-1}\left(\frac{2c_1 d_1}{(c_1^2 - d_1^2)}\right)$$

$$S_1' = 0$$

$$S_2' = 0$$

$$C_1' = \frac{a_1(\kappa - b_1 \mathrm{i})}{\kappa\sqrt{c_1^2 + d_1^2}}$$

$$C_2' = -\frac{a_1\left((\kappa^2 - b_1^2)\mathrm{i} + 2b_1\kappa\right)}{(c_1^2 + d_1^2)\kappa}$$

References

Allen, A.O., 1978. Probability, Statistics, and Queueing Theory. Academic Press, Orlando, Florida.

Arbaret, L., Diot, H., Bouchez, J.-L., 1996. Shape fabrics of particles in low concentration suspension: 2D analogue experiments and application to tiling in magma. Journal of Structural Geology 18, 941–950.

Czeck, D.M., Hudleston, P.J., 2003. Testing models for obliquely plunging lineations in transpression: a natural example and theoretical discussion. Journal of Structural Geology 25, 959–982.

Devore, J.L., 1995. Probability and Statistics for Engineering and the Sciences. Duxbury Press, Pacific Grove, 743 pp.

Fernandez, A., 1987. Preferred orientation developed by rigid markers in two dimensional simple shear – a theoretical and experimental study. Tectonophysics 136, 151–158.

Fernandez, A., Febesse, J.L., Mezure, J.F., 1983. Theoretical and experimental study of fabrics developed by different shaped markers in two-dimensional simple shear. Bulletin de la Société géologique de France 25, 319–326.

Fisher, N.I., 1993. Statistical Analysis of Circular Data. Cambridge University Press, Cambridge, UK.

Ghosh, S.K., 1987. Measure of non-coaxiality. Journal of Structural Geology 9, 111–113.

Ildefonse, B., Sokoutis, D., Mancktelow, N.S., 1992a. Mechanical interactions between rigid particles in a deforming ductile matrix. Analogue experiments in simple shear flow. Journal of Structural Geology 14, 1253–1266.

Ildefonse, B., Launeau, P., Bouchez, J.-L., Fernandez, A., 1992b. Effect of mechanical interactions on the development of shape preferred orientations: a two-dimensional experimental approach. Journal of Structural Geology 14, 73–83.

Jeffery, G.B., 1922. The motion of ellipsoidal particles immersed in a viscous fluid. Proceedings of the Royal Society of London A 102, 201–211.

Jezek, J., Schulmann, K., Segeth, K., 1996. Fabric evolution of rigid inclusions during mixed coaxial and simple shear flows. Tectonophysics 257, 203–221.

Jezek, J., Saic, S., Segeth, K., Schulmann, K., 1999. Three-dimensional hydrodynamical modelling of viscous flow around a rotating ellipsoidal inclusion. Computers and Geosciences 25, 547–558.

Mardia, K.V., 1972. Statistics of Directional Data. Academic Press, London.

Marques, F.O., Coelho, S., 2003. 2-D shape preferred orientations of rigid particles in transtensional viscous flow. Journal of Structural Geology 25, 841–854.

Masuda, T., Kugimiya, Y., Aoshima, I., Hara, Y., Ikei, H., 1999. A statistical approach to determination of a mineral lineation. Journal of Structural Geology 21, 467–472.

Masuda, T., Michibayashi, K., Ohta, H., 1995. Shape preferred orientation of rigid particles in a viscous matrix: reevaluation to determine kinematic parameters of ductile deformation. Journal of Structural Geology 17, 115–129.

Means, W.D., Hobbs, B.E., Lister, G.S., Williams, P.F., 1980. Vorticity and non-coaxiality in progressive deformations. Journal of Structural Geology 2, 371–378.

Meere, P.A., Mulchrone, K.F., 2003. The effect of sample size on geological strain estimation from passively deformed clastic sedimentary rocks. Journal of Structural Geology 25, 1587–1595.

Mulchrone, K.F., 2002. A statistic for estimating strain with confidence intervals from deformed line distributions with an application to schists and gneisses of the Western Gneiss Region, west central Norway. Journal of Structural Geology 24, 545–556.

Mulchrone, K.F., Grogan, S., De, Prithwijit, 2005. The relationship between magmatic tiling, fluid flow and crystal fraction. Journal of Structural Geology 27, 179–197.

Passchier, C.W., 1997. The fabric attractor. Journal of Structural Geology 19, 113–127.

Piazolo, S., Bons, P.D., Passchier, C.W., 2002. The influence of matrix rheology and vorticity on fabric development of populations of rigid objects during plane strain deformation. Tectonophysics 351, 315–329.

Ramberg, H., 1975. Particle paths, displacement and progressive strain applicable to rocks. Tectonophysics 28, 1–35.

Ramsay, J.G., 1967. Folding and Fracturing of Rocks. McGraw-Hill, New York.

Robin, P.F., 1977. Determination of geologic strain using randomly oriented strain markers of any shape. Tectonophysics 42, T7–T16.

Shimamoto, T., Ikeda, Y., 1976. A simple algebraic method for strain estimation from deformed eillipsoidal objects. 1. Basic theory. Tectonophysics 36, 315–337.

Sommerville, D.M.Y., 1949. Analytical Conics, third ed. G. Bell and Sons, London.

Tikoff, B., Fossen, H., 1995. The limitations of three-dimensional kinematic vorticity analysis. Journal of Structural Geology 17, 1771–1784.